

# (U)NFV: Supervised and Unsupervised Neural Finite Volume Methods for Solving Hyperbolic PDEs

Nathan Lichtlé<sup>1,\*</sup>, Alexi Canesse<sup>1,\*</sup>, Zhe Fu<sup>1,\*</sup>, Hossein Nick Zinat Matin<sup>1,\*</sup>,  
Maria Laura Delle Monache<sup>1</sup>, and Alexandre M. Bayen<sup>1</sup>

<sup>1</sup>University of California, Berkeley

<sup>\*</sup>Equal contribution

[lichtle@berkeley.edu](mailto:lichtle@berkeley.edu), [alexi.canesse@berkeley.edu](mailto:alexi.canesse@berkeley.edu),  
[zhefu@berkeley.edu](mailto:zhefu@berkeley.edu), [h-matin@berkeley.edu](mailto:h-matin@berkeley.edu),  
[mldellemonache@berkeley.edu](mailto:mldellemonache@berkeley.edu), [bayen@berkeley.edu](mailto:bayen@berkeley.edu)

**Code, dataset and trained models:** [github.com/nathanlct/nfv](https://github.com/nathanlct/nfv)  
**Supplementary material and videos:** [nathanlichtle.com/research/nfv](https://nathanlichtle.com/research/nfv)

## Abstract

We introduce (U)NFV, a modular neural network architecture that generalizes classical finite volume (FV) methods for solving hyperbolic conservation laws. Hyperbolic partial differential equations (PDEs) are challenging to solve, particularly conservation laws whose physically relevant solutions contain shocks and discontinuities. FV methods are widely used for their mathematical properties: convergence to entropy solutions, flow conservation, or total variation diminishing, but often lack accuracy and flexibility in complex settings. *Neural Finite Volume* addresses these limitations by learning update rules over extended spatial and temporal stencils while preserving conservation structure. It supports both supervised training on solution data (NFV) and unsupervised training via weak-form residual loss (UNFV). Applied to first-order conservation laws, (U)NFV achieves up to **10x lower error** than Godunov's method, outperforms ENO/WENO, and rivals discontinuous Galerkin solvers with far less complexity. On traffic modeling problems, both from PDEs and from experimental highway data, (U)NFV captures nonlinear wave dynamics with significantly higher fidelity and scalability than traditional FV approaches.

## 1 Introduction

*Hyperbolic* partial differential equations (PDEs) [1] are fundamental tools to model propagation and transport phenomena with nonlinear or discontinuous behavior, appearing in areas like fluid dynamics and traffic flow. In the present work, we focus on an essential subclass: *conservation laws* [2], which encode the principle that certain physical quantities, such as mass, momentum, or energy, must be preserved over time. A general one-dimensional scalar conservation law takes the form:

$$\partial_t u(x, t) + \partial_x f(u(x, t)) = 0, \quad (1)$$

where  $u$  is the conserved quantity and  $f$  is the *flux function*.

The solutions of hyperbolic PDEs are difficult to approximate due to discontinuities such as shocks (see Figure 1), even when starting from smooth initial conditions. Consequently, classical (smooth) solutions typically cease to exist after finite time, and one must instead

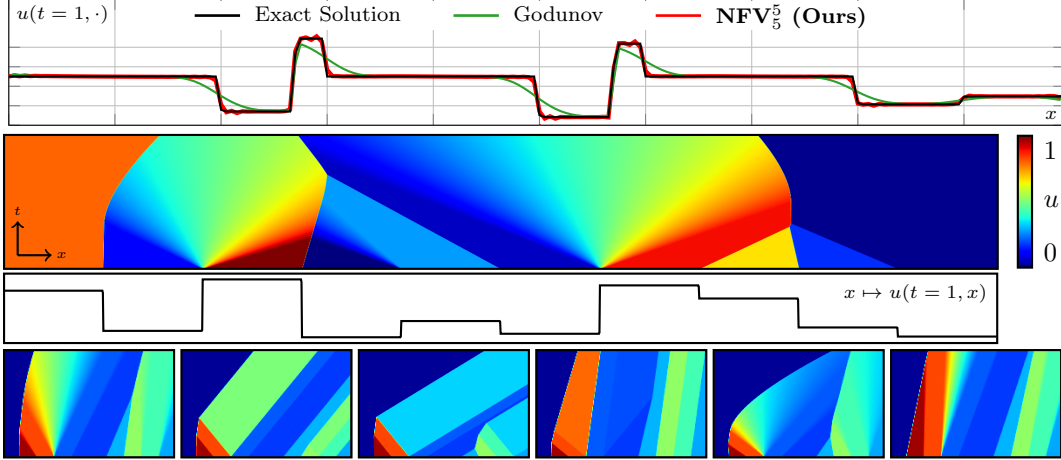


Figure 1: **Prediction of entropy solutions of hyperbolic PDEs.** **Top:**  $\text{NFV}_5^5$  prediction vs. the Godunov scheme for Burgers’ equation at a fixed time. **Mid:** Entropic solution  $u(t, x)$  for Burgers’ equation over domain  $(t, x) \in [0, 1]^2$ , and its corresponding initial condition. **Bottom:** Entropic solution  $u(t, x)$  for the LWR equation with different fluxes sharing the same initial condition.

rely on weak solutions. Closed-form solutions exist only in rare cases, such as on simple Riemann problems [2] or through the Lax-Hopf formula [3–5] in specific concave or convex settings. As a result, practical applications almost always rely on numerical methods for approximating the PDE solution, with finite volume (FV) methods [2] being a popular choice due to their ability to track conserved quantities across discontinuities and capture shock dynamics relatively accurately.

Classical FV methods involve important trade-offs between accuracy near discontinuities, computational cost, stencil size, and implementation complexity. In recent years, neural networks have been explored as flexible and powerful alternatives solvers, showing promise in learning complex dynamics from data or residuals. Yet, many such methods are designed for non-specific models, often at the expense of losing physical structure, including conservation laws and entropy behavior.

We introduce the *Neural Finite Volume* (NFV) method, a modular architecture tailored to conservation laws, that blends the structure-preserving benefits of FV schemes with the expressiveness of neural networks. Conservation is built into the NFV model, using extended spatial and temporal stencils. We develop both a supervised version, trained on solution data from simple cases, and an unsupervised variant (UNFV), which learns directly from the PDE via a weak-form residual loss. This flexibility allows (U)NFV to adapt to the availability of data, leveraging accurate synthetic or field data when present, or solving directly from the equation when solutions are inaccurate or expensive to obtain.

**Contributions.** Our main contributions are as follows:

- We propose (U)NFV, a neural architecture that generalizes the structure of finite volume methods and thus preserves conservation properties by construction.
- We introduce two variants: a supervised learning one (NFV) and an unsupervised learning one (UNFV), depending on data availability, using either solution data or a weak-form residual loss.
- We demonstrate strong numerical results on several conservation laws, achieving up to 10x lower error than classical FV solvers. Additionally, (U)NFV matches the accuracy of discontinuous Galerkin methods, without their mathematical complexity.
- We show that NFV can be trained on field data that does not necessarily strictly satisfy

the conservation law, and still predicts accurate solutions with more flexibility and generalizability than classical solvers.

The remainder of the article is organized as follows: Section 2 provides a detailed overview of the related work, Section 3 recalls the finite volume method and introduces necessary notation, Section 4 describes the proposed (U)NFV method in detail, Section 5 presents the experiments and results on hyperbolic PDEs, Section 6 extends the NFV to experimental field highway data, and Section 7 concludes the article with discussion on broader impacts. Then, Appendix A provides details about finite volume schemes, Appendix B illustrates six PDE variants considered in this work, Appendix C introduces more general PDE models, Appendix D expands on the experimental data handling and results from Section 6, and Appendix E details the experimental setup.

## 2 Related work

**Numerical methods.** Classical numerical methods for hyperbolic PDEs, such as FV and *discontinuous Galerkin* (DG) [6] methods, are widely used due to their capabilities in capturing shocks and discontinuities. First-order schemes such as the *Lax-Friedrichs* [7] and *Godunov* [8] methods provide robustness but suffer from excessive numerical diffusion, leading to smeared solutions. To address this, higher-order methods like *Essentially Non-Oscillatory* (ENO) [9], *Weighted ENO* (WENO) [10], and DG have been introduced, offering improved accuracy in smooth regions while preserving stability near shocks. DG further improves accuracy through local polynomial approximations but incurs high computational costs [11]. Despite their accuracy, these methods often require extensive manual effort and careful stabilization, motivating the development of flexible, data-driven alternatives.

**NN approaches for PDEs.** Deep learning has emerged as a powerful alternative for approximating PDE solutions. In supervised settings, neural operators such as *Fourier Neural Operator* (FNO) [12] and *Deep Operator Networks* (DeepONet) [13] efficiently approximate solution mappings from parametric inputs, without requiring explicit mesh discretization in the case of FNO. While successful for general PDEs, these operators have mainly been validated on elliptic or parabolic PDEs, typically characterized by smooth solutions. Conventional neural architectures, such as CNNs [14] for structured domains and GNNs [15] for irregular geometries, have also been adopted as supervised surrogates. However, supervised models rely heavily on large, high-quality labeled datasets, and often lack intrinsic enforcement of physical constraints, leading to limited generalization and poor accuracy on PDEs involving sharp gradients or shocks [16]. To reduce data reliance, unsupervised approaches like *Physics-Informed Neural Networks* (PINNs) incorporate PDE residuals directly into training losses [17], proving effective for elliptic and parabolic equations [18, 19]. However, PINNs encounter significant difficulties with hyperbolic PDEs, especially in capturing discontinuities and shock dynamics, resulting in unstable optimization, convergence failures, and inaccurate solutions [20, 21]. Recent variants, such as *Weak PINNs* (wPINNs) [22], *Parareal PINNs* (PPINNs) [23], and *Extended PINNs* (XPINNs) [24], aim to overcome these issues through weak formulations or specialized training strategies. Nonetheless, these adaptations often introduce considerable complexity and require extensive hyperparameter tuning, highlighting a persistent need for methods inherently suited to hyperbolic PDE challenges.

**NNs for hyperbolic PDEs/conservation laws.** Neural approaches tailored to hyperbolic PDEs have introduced innovations to handle shocks. Weak PINNs (wPINNs) [22] integrate weak-form residuals or integral constraints to mitigate issues with discontinuities. Others employ neural networks directly within classical FV schemes to learn improved flux reconstructions [25, 26]. However, these enhancements typically reintroduce complexity, such as extensive manual parameterization or problem-specific adaptivity, diluting the key advantage of neural flexibility and generality.

$u_1^4$	$u_2^4$	$u_3^4$	$u_4^4$	$u_5^4$
$u_1^3$	$u_2^3$	$u_3^3$	$u_4^3$	$u_5^3$
$u_1^2$	$u_2^2$	$H_{2,5}^2 u_3^2$	$F_{3,5}^2 u_4^2$	$u_5^2$
$u_1^1$	$u_2^1$	$u_3^1$	$u_4^1$	$u_5^1$

Figure 2: Example stencil for  $\text{FV}_5^2$ , which takes in a rectangular stencil of 2 time steps times 5 space cells to compute the next cell average (in red) using Equation (3) (specifically, both the in-flow and out-flow are computed using the illustrated 2x4 sub-stencils).

Motivated by these limitations, our proposed NFV approach learns local update rules directly from data or PDE residuals. By preserving the fundamental conservation-law structure of traditional FV methods while flexibly leveraging neural networks, NFV achieves significantly higher accuracy, robustness, and scalability with minimal manual intervention.

### 3 Prerequisites and Notations: Finite Volume Methods

Standard FV methods, such as presented in LeVeque [2], solve the integral form of the conservation law (1) on a mesh of uniform cells  $I_i = [x_{i-1/2}, x_{i+1/2}]$ ,  $i = 1, \dots, I_{\max}$ , with cell length  $\Delta x$ . The average of  $u$  over cell  $I_i$  at time  $t_n = n\Delta t$ ,  $n = 1, \dots, N$ , and the numerical flux through the interface  $x_{i+1/2}$  over the time step, are given respectively by

$$u_i^n = \frac{1}{\Delta x} \int_{I_i} u(t_n, x) dx \quad \text{and} \quad F_{i+1/2}^n = \int_{t_n}^{t_{n+1}} f(u(t, x_{i+1/2})) dt, \quad (2)$$

where  $\Delta t$  is the time discretization. A first-order method  $\mathcal{F}$  approximates the numerical flux as  $\hat{F}_{i+1/2}^n = \mathcal{F}(u_i^n, u_{i+1}^n)$ , while higher-order methods leverage additional cell averages.

Let us generalize this framework by including cell averages from previous time steps in order to construct even better approximations. Let  $\text{FV}_a^b$  be the class of methods that use a rectangular stencil of  $a$  neighboring spatial cells times  $b$  past time steps to estimate numerical fluxes. Specifically, let  $\mathbf{u}_{i\pm 1/2}^n(a-1, b)$  be the left and right  $(a-1) \times b$  sub-stencils, as illustrated in blue and green in Figure 2. Then, an  $\text{FV}_a^b$  method  $\mathcal{F}$  estimates numerical fluxes as  $\hat{F}_{i\pm 1/2}^n = \mathcal{F}(\mathbf{u}_{i\pm 1/2}^n(a-1, b))$ . Classical first-order methods, such as Godunov, fall under class  $\text{FV}_3^1$ ; more details about their computation are provided in Appendix A. To our knowledge, the vast majority of FV methods in the literature use a single time step (i.e.,  $b = 1$ ) and a small number of spatial cells space cells. Indeed, designing analytical schemes with larger temporal or spatial stencils becomes exponentially more complex. Finally, the update rule is given by the exact relation

$$u_i^{n+1} = u_i^n - \frac{\Delta t}{\Delta x} (F_{i+1/2}^n - F_{i-1/2}^n), \quad (3)$$

which in practice is approximated using the numerical fluxes  $\hat{F}_{i\pm 1/2}^n$ , leading to an approximation  $\hat{u}_i^n$  of  $u_i^n$ . Note that the influx of one cell is the outflux of another, which ensures conservation.

### 4 Our method: Neural Finite Volume (NFV)

Our method builds upon the FV framework by using neural networks to approximate the numerical flux. Specifically, we define  $\text{NFV}_a^b$  as a generalization of  $\text{FV}_a^b$ , where the numerical flux  $\hat{F}_{i\pm 1/2}^n$  is predicted by a neural network  $\mathcal{N}$  based on a local  $a \times b$  spatiotemporal stencil:

$$\hat{F}_{i\pm 1/2}^n = \mathcal{N}(\mathbf{u}_{i\pm 1/2}^n(a-1, b))$$

The prediction of the solution is then updated using the classical FV update rule (3), ensuring mass conservation. We explore NFV models ranging from  $\text{NFV}_3^1$  (matching Godunov's stencil) to  $\text{NFV}_{11}^{11}$ , using 11 spatial cells and 11 past time steps – configurations that would be exceedingly complex to design manually due to the high-dimensional stencil involved. This extension enables accurate learning even from noisy field data. In practice, we implement NFV as a CNN [14], which allows efficient computation across stencils due to the vectorized nature of CNNs. We refer to Appendix E for implementation details.

We propose two variants: the supervised  $\text{NFV}_a^b$ , trained on solution data, and the unsupervised  $\text{UNFV}_a^b$ , trained directly from the PDE via a weak-form residual loss. Both share the same neural network architecture and only differ in their training objective. This framework is thus designed to be adapted to different kinds of problems.

## 4.1 Learning Objectives: Supervised and Unsupervised

Solving hyperbolic PDEs presents unique challenges, particularly due to the absence of closed-form solutions, even under simple initial conditions. To address this, we propose two distinct learning objectives: supervised and unsupervised. The supervised objective is applicable when reference solutions are available. Conversely, the unsupervised objective is employed when such solutions are unavailable, allowing the model to infer solutions by adhering to the underlying physical laws. Notably, supervised learning can also be utilized in scenarios where the governing equations are unknown, provided that observational data is accessible. This approach facilitates the application of numerical solvers to empirical data, imposing only fundamental physical constraints, such as mass conservation, without requiring extensive hyperparameter tuning (see Section 6).

### 4.1.1 Supervised Learning

Supervised learning offers a straightforward framework for training models when reference solutions are available. In this study, we employ supervised learning not only to approximate the solution of known equations but also to predict field data with unknown governing equations. Although solutions to hyperbolic PDEs are typically defined in the  $L_1$  space, we consider their restrictions to compact subsets where the functions are bounded, thereby allowing treatment within the  $L_2$  space. Accordingly, the loss function is defined as the standard mean square error:

$$\mathcal{L}_s = \mathbb{E}_{u_0 \sim \mathcal{R}} \|u - \hat{u}\|_2^2$$

where  $u$  is the true solution,  $\hat{u}$  is the predicted solution, and  $\mathcal{R}$  is a distribution over initial conditions.

### 4.1.2 Unsupervised Learning

Unsupervised learning for hyperbolic PDEs is inherently more challenging due to the nature of their solutions. Closed-form solutions rarely exist, even for simple cases, and classical (strong) solutions often do not exist altogether. As a result, these equations are typically solved in a weak form. However, weak solutions are not unique, as multiple solutions can satisfy the PDE, but only one adheres to the entropy condition, making it physically meaningful.

The unsupervised loss function is defined to minimize the residuals of the weak formulation, in order to approximate the entropic solution. While imposing this loss does not guarantee convergence to the entropic solution, empirical results indicate that our method successfully converges to the entropy solution across various equations and numerous trials. To enhance learning efficiency, we optimize the weak formulation independently at each time step by minimizing the squared residuals. The collection of test functions  $\Phi$  consists of 250 randomly sampled, compactly supported polynomials of degree 50 over the spatial domain. The

Table 1: Performance comparison between neural network models and classical numerical schemes. Results are computed over the evaluation set of 1000 piecewise constant initial conditions. For each method, we report mean and standard deviation in  $L_2$  norm (mean( $(u - \hat{u})^2$ )).

	1 <sup>st</sup> order FV				Higher order FV			FEM
	NFV <sub>3</sub> <sup>1</sup>	UNFV <sub>3</sub> <sup>1</sup>	GD	LF	EO	ENO	WENO	DG
G.shields	<b>1.3e<sup>-4</sup><sub>± 4e<sup>-5</sup></sub></b>	2.0e <sup>-4</sup> <sub>± 6e<sup>-5</sup></sub>	4.5e <sup>-4</sup> <sub>± 2e<sup>-4</sup></sub>	1.3e <sup>-2</sup> <sub>± 4e<sup>-3</sup></sub>	4.5e <sup>-4</sup> <sub>± 2e<sup>-4</sup></sub>	6.4e <sup>-4</sup> <sub>± 4e<sup>-4</sup></sub>	6.4e <sup>-4</sup> <sub>± 4e<sup>-4</sup></sub>	3.1e <sup>-5</sup> <sub>± 1e<sup>-5</sup></sub>
Tri. 1	<b>1.4e<sup>-3</sup><sub>± 6e<sup>-4</sup></sub></b>	1.9e <sup>-3</sup> <sub>± 9e<sup>-4</sup></sub>	2.3e <sup>-3</sup> <sub>± 1e<sup>-3</sup></sub>	9.6e <sup>-3</sup> <sub>± 4e<sup>-3</sup></sub>	2.3e <sup>-3</sup> <sub>± 1e<sup>-3</sup></sub>	2.0e <sup>-3</sup> <sub>± 2e<sup>-3</sup></sub>	1.9e <sup>-3</sup> <sub>± 2e<sup>-3</sup></sub>	2.6e <sup>-4</sup> <sub>± 1e<sup>-4</sup></sub>
Tri. 2	<b>2.4e<sup>-3</sup><sub>± 1e<sup>-3</sup></sub></b>	3.1e <sup>-3</sup> <sub>± 2e<sup>-3</sup></sub>	3.8e <sup>-3</sup> <sub>± 2e<sup>-3</sup></sub>	1.4e <sup>-2</sup> <sub>± 8e<sup>-3</sup></sub>	3.8e <sup>-3</sup> <sub>± 2e<sup>-3</sup></sub>	5.8e <sup>-3</sup> <sub>± 4e<sup>-3</sup></sub>	5.8e <sup>-3</sup> <sub>± 4e<sup>-3</sup></sub>	4.1e <sup>-4</sup> <sub>± 2e<sup>-4</sup></sub>
Trapez.	<b>1.1e<sup>-3</sup><sub>± 4e<sup>-4</sup></sub></b>	1.6e <sup>-3</sup> <sub>± 7e<sup>-4</sup></sub>	2.1e <sup>-3</sup> <sub>± 8e<sup>-4</sup></sub>	2.5e <sup>-2</sup> <sub>± 1e<sup>-2</sup></sub>	2.1e <sup>-3</sup> <sub>± 8e<sup>-4</sup></sub>	6.2e <sup>-4</sup> <sub>± 2e<sup>-4</sup></sub>	5.3e <sup>-4</sup> <sub>± 2e<sup>-4</sup></sub>	2.9e <sup>-4</sup> <sub>± 1e<sup>-4</sup></sub>
G.berg	<b>1.4e<sup>-4</sup><sub>± 9e<sup>-5</sup></sub></b>	3.8e <sup>-4</sup> <sub>± 2e<sup>-4</sup></sub>	4.9e <sup>-4</sup> <sub>± 2e<sup>-4</sup></sub>	5.3e <sup>-3</sup> <sub>± 2e<sup>-3</sup></sub>	4.9e <sup>-4</sup> <sub>± 2e<sup>-4</sup></sub>	1.1e <sup>-3</sup> <sub>± 6e<sup>-4</sup></sub>	1.2e <sup>-3</sup> <sub>± 9e<sup>-4</sup></sub>	3.4e <sup>-4</sup> <sub>± 2e<sup>-3</sup></sub>
U.wood	<b>3.8e<sup>-4</sup><sub>± 1e<sup>-4</sup></sub></b>	6.9e <sup>-4</sup> <sub>± 2e<sup>-4</sup></sub>	9.2e <sup>-4</sup> <sub>± 3e<sup>-4</sup></sub>	2.7e <sup>-2</sup> <sub>± 1e<sup>-2</sup></sub>	9.2e <sup>-4</sup> <sub>± 3e<sup>-4</sup></sub>	1.1e <sup>-4</sup> <sub>± 3e<sup>-5</sup></sub>	9.8e <sup>-5</sup> <sub>± 2e<sup>-5</sup></sub>	5.9e <sup>-5</sup> <sub>± 2e<sup>-5</sup></sub>
Burgers	<b>8.5e<sup>-4</sup><sub>± 3e<sup>-4</sup></sub></b>	1.3e <sup>-3</sup> <sub>± 6e<sup>-4</sup></sub>	1.9e <sup>-3</sup> <sub>± 7e<sup>-4</sup></sub>		2.6e <sup>-3</sup> <sub>± 1e<sup>-3</sup></sub>	2.7e <sup>-3</sup> <sub>± 1e<sup>-3</sup></sub>	2.8e <sup>-3</sup> <sub>± 1e<sup>-3</sup></sub>	1.0e <sup>-4</sup> <sub>± 4e<sup>-5</sup></sub>

unsupervised loss reads:

$$\mathcal{L}_w = \mathbb{E}_{\substack{\varphi \in \Phi \\ u_0 \sim \mathcal{R}}} \left[ \sum_{n=1}^N \left( \sum_{i=1}^{I_{\max}} \left( (\Delta t)^{-1} (\hat{u}_i^n - \hat{u}_i^{n-1}) \int_{I_i} \varphi + f(\hat{u}_i^n) [\varphi]_{x_{i-1/2}}^{x_{i+1/2}} \right) \right)^2 \right]$$

where  $\hat{u}_i^n$  denotes the predicted solution at spatial index  $i$  and time step  $n$ , and  $\mathcal{R}$  is a distribution over initial conditions.

## 5 Experiments

Experiments have been designed to answer four main questions:

- Is (U)NFV a compelling alternative to classical finite volume methods?
- Does UNFV converge to an entropic solution despite being trained on the weak formulation?
- How does (U)NFV compare to much more complicated finite element methods?
- Can NFV perform well on field data that contains noise and may not be conservative?

### 5.1 Baselines

Selecting appropriate baselines for PDE solvers poses challenges due to the diversity in computational frameworks: methods vary by mesh dependency (mesh-free versus mesh-based), solution generation (autoregressive versus single-pass), and generalizability (operator-based versus retrained per initial condition). Therefore, we adopt classical numerical schemes, the foundation of our NFV method, as baselines, ensuring a fair comparison. Given the fact that NFV is developed based on traditional first-order FV methods, the present work provides a compelling case for replacing standard FV solvers with the simpler yet effective NFV method whenever FV methods are typically employed. We consider all the numerical schemes introduced in Section 2 as baselines: first-order FV methods (Godunov, Lax-Friedrichs, and Engquist-Osher), higher-order ones (ENO, WENO), and DG, a finite-element method that is well-known for superior accuracy but suffers from computational burden. More details can be found in Appendix A.

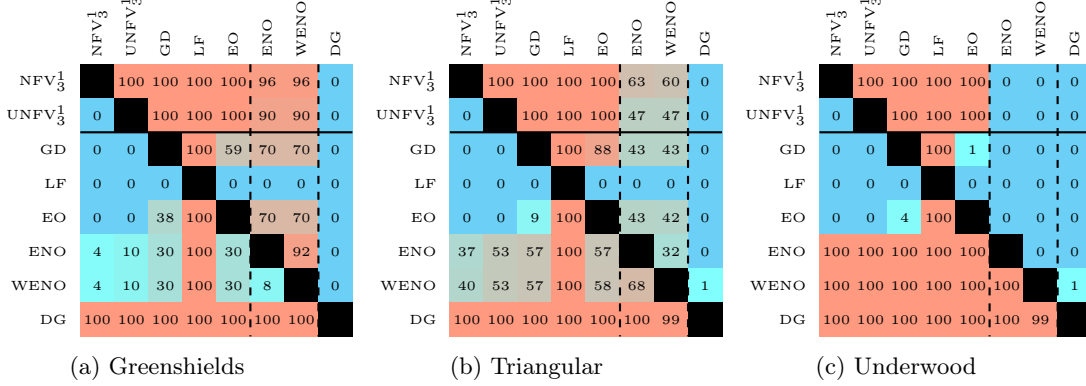


Figure 3: **Comparison of numerical schemes across flow functions.** Each cell shows the proportion of the evaluation set on which the row scheme outperforms the column scheme. DG, the only FEM tested, is rarely beaten. NFV<sub>3</sub><sup>1</sup> and UNFV<sub>3</sub><sup>1</sup> outperform other first-order schemes and rival higher-order ones, making them strong choices depending on the equation.

## 5.2 Equations

The Lighthill-Whitham-Richards model [27, 28], known as LWR, is a first-order hyperbolic conservation law used to model traffic flow. It is expressed as

$$\partial_t \rho + \partial_x(\rho v(\rho)) = 0 \quad (4)$$

ewhere  $\rho$  is the density of the traffic,  $f : \rho \mapsto \rho v(\rho)$  is the flux function and  $v$  is the velocity. The flux function is typically modeled as a concave function of the density. Variations in the underlying velocity function give rise to different traffic flow models. In this work, six different models have been considered: Greenshields' [29], Triangular [30], Triangular skewed [30], Trapezoidal [31], Greenberg [32] and Underwood [33]. These models behave *very* differently and should be considered as different equations, as shown in Figure 1. Formulations and illustrations of those six models are given in Appendix B.

The inviscid Burgers' equation is a well-known hyperbolic conservation law used in various domains such as fluid mechanics [34], non-linear acoustics [35], gas dynamics [36], and traffic flow [37]. We refer the reader to Cameron [38] for a thorough introduction. It is expressed as

$$\partial_t u + \frac{1}{2} \partial_x u^2 = 0. \quad (5)$$

This equation can be written in the classical form of a conservation law using the flux function  $f : u \mapsto 1/2 \cdot u^2$ . Exact solutions to Riemann initial conditions are also known for this problem. Visualization of some solutions, including videos, are available on our webpage and in Figure 1.

While we focus on one-dimension equations in this work, our methods are, at least theoretically, generalizable to the multi-dimensional case of conservation laws [39]. In addition, we expect that our proposed methods can be extended to second-order hyperbolic equations such as ARZ-type models [40, 41] and shallow water equations [2]; see Appendix C for details.

## 5.3 Datasets

Training is performed using solutions derived from Riemann problems, which are initial value problems characterized by piecewise constant initial conditions with a single discontinuity (see Figure 8 for examples). These problems are fundamental in the study of hyperbolic PDEs and serve as essential test cases for numerical methods. For the scenarios considered in this work, analytical solutions to Riemann problems are available, making supervised

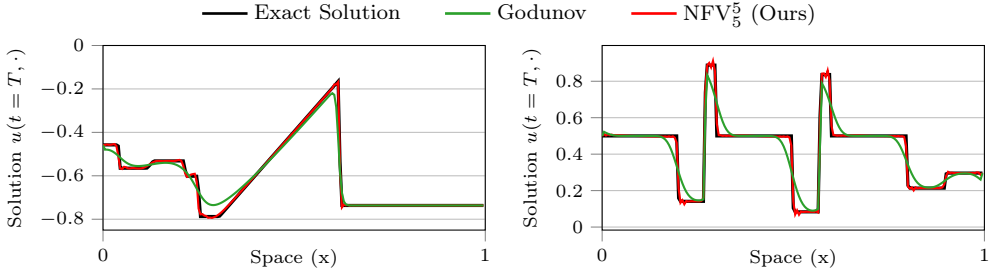


Figure 4: Comparison of the final density of the Burgers’ equation (left) and LWR triangular equation (right) for  $\text{NFV}_5^5$  and the Godunov Scheme. The proposed method displays an excellent approximation of the exact solution, capturing sharp features such as discontinuities and points of non-differentiability. It contains some minor oscillations in the solution, which are not present in the Godunov scheme. The latter, however, fails to capture the discontinuities and points of non-differentiability, offering a very smoothed solution.

learning possible. Evaluation is performed on a more complicated set of a several hundred initial conditions to assess the model’s generalization capabilities. These conditions consist of piecewise constant functions with ten discontinuities, introducing increased complexity. Exact solutions for these test cases are computed using the Lax-Hopf algorithm [3–5] on a finer grid (see Appendix E).

#### 5.4 Results and discussion

Table 1 reports  $L_2$  error for  $\text{NFV}_3^1$ ,  $\text{UNFV}_3^1$ , and baseline methods across the seven benchmark equations. Our models consistently outperform all first-order FV methods, and surpass ENO/WENO schemes on about half of the equations. As expected, the higher-order DG method achieves significantly lower errors. Table 2 shows that  $\text{NFV}_5^5$ , while as simple to implement as standard  $\text{NFV}_3^1$ , achieves up to 10x better accuracy, approaching the performance of DG.

Figure 3 shows the fraction of test cases each method wins.  $\text{NFV}_3^1$  and  $\text{UNFV}_3^1$  consistently surpass first-order FV methods. Against ENO/WENO, performance varies: our models outperform on some equations, match on others, and underperform in a few, highlighting the complexity of benchmarking across diverse problem settings. Still, the fact that  $\text{NFV}_3^1$  and  $\text{UNFV}_3^1$  consistently do better than first-order methods is seen as a sign that the approach appears to converge well. Specifically,  $\text{NFV}_3^1$  and  $\text{UNFV}_3^1$  consistently produce errors bounded by those of Godunov, emphasizing their robustness.

Since all methods use autoregressive prediction, evaluating performance at the final time step provides a good proxy for cumulative error. Figure 4 shows that the prediction of  $\text{NFV}_5^5$  closely aligns with the exact solution, with only minor oscillations observed. Notably,  $\text{NFV}_5^5$  effectively captures sharp discontinuities with high accuracy without relying on smoothing techniques, which are commonly employed in traditional FV methods to mitigate numerical artifacts.

A strong strength of classical numerical schemes is their proven convergence when the discretization is refined. While this is not proven for our method, Figure 5 shows that both  $\text{NFV}_3^1$  and  $\text{UNFV}_3^1$  can consistently perform better than Godunov, a scheme proven to converge, even when the grid is refined. Our schemes are thus expected to converge. The log-log plot exhibits a linear trends, which suggests that the rate of convergence could be polynomial.

Table 2: Evaluation of  $\text{NFV}_5^5$  using piecewise constant initial conditions. Error is reported in  $L_2$  norm.  $\text{NFV}_5^5$  achieve outstanding performance, gaining up to an order of magnitude improvement compared to Godunov and WENO. Its performance is close to DG, while keeping the implementation simplicity of a finite volume method and the computational complexity of NFV.

	Godunov	WENO	$\text{NFV}_3^1$	$\text{NFV}_5^5$	DG
Burgers'	$1.8e^{-3}_{\pm 6e^{-4}}$	$2.6e^{-3}_{\pm 1e^{-3}}$	$8.3e^{-4}_{\pm 3e^{-4}}$	$2.2e^{-4}_{\pm 1e^{-4}}$	$1.0e^{-4}_{\pm 4e^{-5}}$
Greenshields	$4.1e^{-4}_{\pm 1e^{-4}}$	$6.9e^{-4}_{\pm 4e^{-4}}$	$1.2e^{-4}_{\pm 4e^{-5}}$	$4.6e^{-5}_{\pm 3e^{-5}}$	$4.2e^{-5}_{\pm 2e^{-5}}$
Triangular	$2.2e^{-3}_{\pm 1e^{-3}}$	$2.0e^{-3}_{\pm 2e^{-3}}$	$1.3e^{-3}_{\pm 6e^{-4}}$	$2.9e^{-4}_{\pm 2e^{-4}}$	$2.7e^{-4}_{\pm 1e^{-4}}$

## 6 Application: Modeling Large-Scale Experimental Field Data using NFV

We apply the proposed NFV method to large-scale traffic field data collected on Interstate 24 (I-24) in Tennessee, USA, using the I-24 MOTION infrastructure [42, 43], which enables high-resolution vehicle trajectory collection and constitutes the most extensive publicly available traffic dataset to date. Rather than predicting traffic speed, we focus on modeling traffic density, which is more directly tied to conservation laws and often exhibits sharp transitions that are challenging to capture. Although conservation of mass is not strictly satisfied in highway traffic data due to merges, exits, and incidents, it serves as a strong inductive bias. We show that NFV achieves superior predictive accuracy compared to classical numerical schemes. Moreover, incorporating the PDE structure leads to substantially more stable training, particularly in data-scarce regimes. These findings suggest that our approach can enhance the accuracy and efficiency of traffic simulations, thereby contributing to better-informed decision-making in urban planning and traffic management.

### 6.1 Dataset

We evaluate our method on the I-24 MOTION dataset [42], which provides high-resolution vehicle trajectories collected on a four-mile stretch of Interstate 24 (mile markers 58.7 to 62.7) near Nashville, Tennessee. The data is captured by a network of high-definition cameras mounted along the highway as part of the I-24 MOTION infrastructure, leading to intricate trajectory data as illustrated in Figure 9. Vehicle trajectories are reconstructed using a computer vision and data association pipeline [44], resulting in high-fidelity, though inherently noisy, field data.

The dataset consists of 10 days of vehicle trajectory data, collected during the morning rush hour (6:00 AM to 10:00 AM) over the 4-mile segment. From the raw trajectory data, we construct spatiotemporal vehicle density fields by aggregating vehicle counts over fixed spatial cells. Details of the data cleaning, processing, and preparation are provided in Appendix D.1. Visualization of the resulting density fields is shown in Figure 10.

### 6.2 Results and Discussion

We compare NFV to numerical schemes using the flux functions from Appendix B. These functions, each defined by a few parameters, were calibrated via optimization to minimize the Godunov scheme's prediction error on the training set. The search ranges were intentionally broad, prioritizing predictive performance over physical plausibility to ensure a fair comparison. We evaluate three NFV variants of increasing capacity:  $\text{NFV}_3^1$ ,  $\text{NFV}_5^5$ , and  $\text{NFV}_{11}^{11}$  (training details can be found in Appendix E), to assess how well they generalize and capture complex field dynamics.

Table 3 shows that all NFV models outperform the five tuned Godunov schemes, with

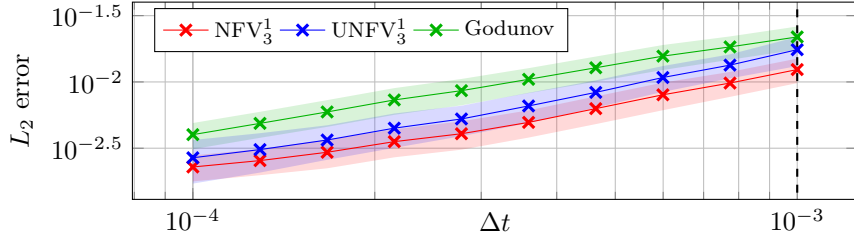


Figure 5: **Convergence plots on Greenshields' flux.** The  $L_2$  error is computed against the exact solution on the evaluation set for different mesh discretizations. We report both error average and standard deviation, on a log-log scale. The dashed vertical line illustrates the discretization on which  $NFV_3^1$  and  $UNFV_3^1$  were trained; the models generalize to smaller discretizations. The ratio  $\Delta t / \Delta x = 0.1$  remains constant as the mesh is refined.

Table 3: **Improvements of NFV at different scales against numerical methods with fitted flow functions on field data.** The reported metrics include  $L_1$  error ( $\text{mean}(|u - \hat{u}|)$ ),  $L_2$  error ( $\text{mean}((u - \hat{u})^2)$ ), and relative error ( $\text{mean}(|u - \hat{u}| / |\max\{\varepsilon, u\}|)$ ). The larger the input size of NFV, the better the performance.  $NFV_3^1$  outperforms all calibrated Godunov fits, despite having the same input size and underlying structure.

	Calibrated numerical schemes (Godunov)					NFV (Ours)		
	Greenshields	Triangular	Trapezoidal	Greenberg	Underwood	$NFV_3^1$	$NFV_5^5$	$NFV_{11}^{11}$
$L_1$	$6.05e^{-2}$	$2.77e^{-2}$	$2.73e^{-2}$	$2.79e^{-2}$	$4.98e^{-2}$	<b><math>2.37e^{-2}</math></b>	$2.31e^{-2}$	<b><math>2.02e^{-2}</math></b>
$L_2$	$1.93e^{-1}$	$1.31e^{-1}$	$1.30e^{-1}$	$1.33e^{-1}$	$1.81e^{-1}$	<b><math>1.23e^{-1}</math></b>	$1.21e^{-1}$	<b><math>1.09e^{-1}</math></b>
Rel.	$5.04e^{-1}$	$3.83e^{-1}$	$3.74e^{-1}$	$3.75e^{-1}$	$5.45e^{-1}$	<b><math>3.57e^{-1}</math></b>	$3.51e^{-1}$	<b><math>2.83e^{-1}</math></b>

performance improving as input size increases. This trend matches what was seen on synthetic data (Section 5). Despite training on just one hour of data, NFV predicts nearly four hours of traffic evolution autoregressively (Figure 6). While performance degrades in out-of-distribution zones (e.g., dark green regions unseen during training), the models still capture key wave patterns with high fidelity. Larger stencils help smooth out noise and improve accuracy, as seen in Figure 13.

We further evaluate generalization on 7 other days. As shown in Figure 14 and Table 4,  $NFV_{11}^{11}$  consistently outperforms the best Godunov scheme on the evaluation set, even though both perform similarly on the training day. Indeed, although far from perfect, it is able to capture the evolution of free-flow traffic (dark green) with much greater accuracy, allowing it to successfully capture the end of congestion waves (red). NFV scales naturally with capacity:  $NFV_{11}^{11}$  adds only 1728 parameters over  $NFV_3^1$  but achieves significantly better accuracy with similar runtime and memory usage, unlike hand-crafted schemes, which significantly grow in complexity (see for example Appendix A).

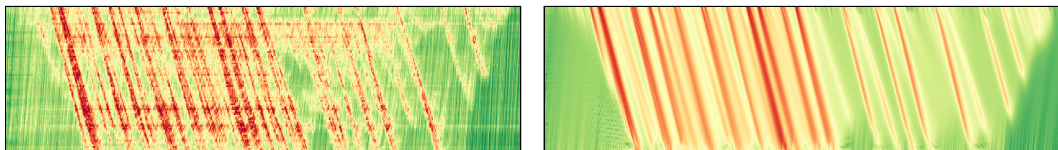


Figure 6: **Autoregressive prediction of  $NFV_{11}^{11}$  (right) compared to the ground truth (left).** Full results are shown in Figure 13. See Appendix D.3 for how to read the heatmaps.

Table 4: **Generalization of NFV against Godunov on 7 days of I-24 data never seen during training.** As in Table 3, we report mean and standard deviation of L1, L2 and relative errors.

	L1 error	L2 error	Relative error
Godunov	$1.56e^{-1} \pm 2.02e^{-2}$	$3.74e^{-2} \pm 8.25e^{-3}$	$6.26e^{-1} \pm 2.58e^{-1}$
NFV <sub>11</sub> <sup>11</sup>	<b><math>1.12e^{-1} \pm 7.39e^{-3}</math></b>	<b><math>2.20e^{-2} \pm 2.59e^{-3}</math></b>	<b><math>3.59e^{-1} \pm 7.58e^{-2}</math></b>

## 7 Conclusion

We introduced a neural network-based framework for solving conservation laws that significantly improves accuracy over classical FV methods, while retaining the simplicity and structure of first-order schemes. Despite these empirical gains, a fundamental limitation remains: NFV and UNFV currently lack the rigorous theoretical guarantees, such as stability and convergence, established for traditional numerical methods. Nonetheless, the proposed approach demonstrates strong practical performance across diverse settings. Looking ahead, several important research directions warrant further exploration. First, establishing theoretical foundations for neural network-based solvers, particularly with respect to convergence and the preservation of physical constraints, is essential. Second, extending the methodology to more complex PDEs and high-dimensional domains will be critical for assessing its scalability and generalizability. Finally, hybrid strategies that integrate data-driven learning with classical numerical techniques may offer enhanced robustness and accuracy, bridging the gap between theoretical rigor and practical flexibility.

**Broader impacts:** The proposed NFV framework has the potential to enhance simulations in domains such as traffic flow, environmental modeling, and fluid dynamics, thereby supporting more informed decision-making in urban planning and infrastructure development. However, reliance on data-driven models without rigorous validation may lead to inaccuracies, potentially resulting in misguided policies or designs. To mitigate such risks, we advocate for thorough validation against empirical data and collaboration with domain experts to ensure responsible application of the technology.

## References

- [1] Lawrence C Evans. *Partial differential equations*, volume 19. American Mathematical Society, 2022.
- [2] Randall J LeVeque. *Finite volume methods for hyperbolic problems*, volume 31. Cambridge university press, 2002.
- [3] PD Lax. Hyperbolic systems of conservation laws ii. *Communications on Pure and Applied Mathematics*, 10(4):537–566, 1957.
- [4] Christian G Claudel and Alexandre M Bayen. Lax–hopf based incorporation of internal boundary conditions into hamilton–jacobi equation. part i: Theory. *IEEE Transactions on Automatic Control*, 55(5):1142–1157, 2010.
- [5] Christian G Claudel and Alexandre M Bayen. Lax–hopf based incorporation of internal boundary conditions into hamilton–jacobi equation. part ii: Computational methods. *IEEE Transactions on Automatic Control*, 55(5):1158–1174, 2010.
- [6] Changqing Hu and Chi-Wang Shu. A discontinuous galerkin finite element method for hamilton–jacobi equations. *SIAM Journal on Scientific computing*, 21(2):666–690, 1999.
- [7] PD Lax. The initial value problem for nonlinear hyperbolic equations in two independent variables. *Ann. Math. Studies*, 33(21):1–229, 1954.

- [8] SK Godunov. A finite difference method for the computation of discontinuous solutions of the equations of fluid dynamics. *Sbornik: Mathematics*, 47(8-9):357–393, 1959.
- [9] Chi-Wang Shu. High order eno and weno schemes for computational fluid dynamics. In *High-order methods for computational physics*, pages 439–582. Springer, 1999.
- [10] Xu-Dong Liu, Stanley Osher, and Tony Chan. Weighted essentially non-oscillatory schemes. *Journal of computational physics*, 115(1):200–212, 1994.
- [11] Bernardo Cockburn and Chi-Wang Shu. The local discontinuous galerkin method for time-dependent convection-diffusion systems. *SIAM Journal on Numerical Analysis*, 35(6):2440–2463, 1998.
- [12] Zongyi Li, Nikola Kovachki, Kamyar Azizzadenesheli, Burigede Liu, Kaushik Bhattacharya, Andrew Stuart, and Anima Anandkumar. Fourier neural operator for parametric partial differential equations. *arXiv preprint arXiv:2010.08895*, 2020.
- [13] Lu Lu, Pengzhan Jin, Guofei Pang, Zhongqiang Zhang, and George Em Karniadakis. Learning nonlinear operators via deeponet based on the universal approximation theorem of operators. *Nature machine intelligence*, 3(3):218–229, 2021.
- [14] Yann LeCun, Yoshua Bengio, et al. Convolutional networks for images, speech, and time series. *The handbook of brain theory and neural networks*, 3361(10):1995, 1995.
- [15] Michael M Bronstein, Joan Bruna, Yann LeCun, Arthur Szlam, and Pierre Vandergheynst. Geometric deep learning: going beyond euclidean data. *IEEE Signal Processing Magazine*, 34(4):18–42, 2017.
- [16] Aditi Krishnapriyan, Amir Gholami, Shandian Zhe, Robert Kirby, and Michael W Mahoney. Characterizing possible failure modes in physics-informed neural networks. *Advances in neural information processing systems*, 34:26548–26560, 2021.
- [17] Maziar Raissi, Paris Perdikaris, and George Em Karniadakis. Physics informed deep learning (part i): Data-driven solutions of nonlinear partial differential equations. *arXiv preprint arXiv:1711.10561*, 2017.
- [18] Maziar Raissi, Paris Perdikaris, and George E Karniadakis. Physics-informed neural networks: A deep learning framework for solving forward and inverse problems involving nonlinear partial differential equations. *Journal of Computational physics*, 378:686–707, 2019.
- [19] Ameya D Jagtap, Ehsan Kharazmi, and George Em Karniadakis. Conservative physics-informed neural networks on discrete domains for conservation laws: Applications to forward and inverse problems. *Computer Methods in Applied Mechanics and Engineering*, 365:113028, 2020.
- [20] Feng Wang and Huaping Liu. Understanding the behaviour of contrastive loss. In *Proceedings of the IEEE/CVF conference on computer vision and pattern recognition*, pages 2495–2504, 2021.
- [21] Olga Fuks and Hamdi A Tchelepi. Limitations of physics informed machine learning for nonlinear two-phase transport in porous media. *Journal of Machine Learning for Modeling and Computing*, 1(1), 2020.
- [22] Tim De Ryck, Siddhartha Mishra, and Roberto Molinaro. wpinns: Weak physics informed neural networks for approximating entropy solutions of hyperbolic conservation laws. *SIAM Journal on Numerical Analysis*, 62(2):811–841, 2024.

- [23] Xuhui Meng, Zhen Li, Dongkun Zhang, and George Em Karniadakis. Ppinn: Parareal physics-informed neural network for time-dependent pdes. *Computer Methods in Applied Mechanics and Engineering*, 370:113250, 2020.
- [24] Ameya D Jagtap and George Em Karniadakis. Extended physics-informed neural networks (xpinns): A generalized space-time domain decomposition based deep learning framework for nonlinear partial differential equations. *Communications in Computational Physics*, 28(5), 2020.
- [25] Tatiana Kossaczká, Matthias Ehrhardt, and Michael Günther. Enhanced fifth order weno shock-capturing schemes with deep learning. *Results in Applied Mathematics*, 12: 100201, 2021.
- [26] Yunjin Tong, Shiying Xiong, Xingzhe He, Shuqi Yang, Zhecheng Wang, Rui Tao, Runze Liu, and Bo Zhu. Roenet: Predicting discontinuity of hyperbolic systems from continuous data. *International Journal for Numerical Methods in Engineering*, 125(6):e7406, 2024.
- [27] Michael James Lighthill and G Be Whitham. On kinematic waves i. flood movement in long rivers. *Proceedings of the Royal Society of London. Series A. Mathematical and Physical Sciences*, 229(1178):281–316, 1955.
- [28] P. I. Richards. Shock waves on the highway. *Operations Research*, 4:42–51, 1956.
- [29] Bruce D Greenshields, J Rowland Bibbins, WS Channing, and Harvey H Miller. A study of traffic capacity. In *Highway research board proceedings*, volume 14, pages 448–477. Washington, DC, 1935.
- [30] Nikolas Geroliminis and Carlos F Daganzo. Existence of urban-scale macroscopic fundamental diagrams: Some experimental findings. *Transportation Research Part B: Methodological*, 42(9):759–770, 2008.
- [31] Nikolas Geroliminis and Jie Sun. Properties of a well-defined macroscopic fundamental diagram for urban traffic. *Transportation Research Part B: Methodological*, 45(3): 605–617, 2011.
- [32] Harold Greenberg. An analysis of traffic flow. *Operations research*, 7(1):79–85, 1959.
- [33] Robin T Underwood. Speed, volume and density relationships. *Quality and theory of traffic flow*, 1961.
- [34] JM Burgers. Math. examples illustrating relations occurring in the theory of turbulent fluid motion. akademie van wetenschappen. *Amsterdam. 1. Sect.*, 17:2, 1939.
- [35] Bruno Lombard, Denis Matignon, and Yann Le Gorrec. A fractional burgers equation arising in nonlinear acoustics: theory and numerics. *IFAC Proceedings Volumes*, 46(23): 406–411, 2013.
- [36] DE Panayotounakos and D Drikakis. On the closed-form solutions of the wave, diffusion and burgers equations in fluid mechanics. *ZAMM-Journal of Applied Mathematics and Mechanics/Zeitschrift für Angewandte Mathematik und Mechanik*, 75(6):437–447, 1995.
- [37] Toshimitsu Musha and Hideyo Higuchi. Traffic current fluctuation and the burgers equation. *Japanese journal of applied physics*, 17(5):811, 1978.
- [38] MARIA Cameron. Notes on the burgers equation. *University of Maryland*, 2011.
- [39] A. Bressan. Leggi di conservazione. *La Matematica nella Società e nella Cultura*, 2003.
- [40] AATM Aw and Michel Rascle. Resurrection of "second order" models of traffic flow. *SIAM journal on applied mathematics*, 60(3):916–938, 2000.

- [41] HM Zhang. Structural properties of solutions arising from a nonequilibrium traffic flow theory. *Transportation Research Part B: Methodological*, 34(7):583–603, 2000.
- [42] Derek Gloudemans, Yanbing Wang, Junyi Ji, Gergely Zachar, William Barbour, Eric Hall, Meredith Cebelak, Lee Smith, and Daniel B Work. I-24 motion: An instrument for freeway traffic science. *Transportation Research Part C: Emerging Technologies*, 155:104311, 2023.
- [43] Derek Gloudemans, Gergely Zachár, Yanbing Wang, Junyi Ji, Matt Nice, Matt Bunting, William Barbour, Jonathan Sprinkle, Benedetto Piccoli, Maria Laura Monache, Alexandre Bayen, Benjamin Seibold, and Daniel B. Work. So you think you can track? *arXiv preprint arXiv:2309.07268*, 2023.
- [44] Yanbing Wang, Derek Gloudemans, Zi Nean Teoh, Lisa Liu, Gergely Zachár, William Barbour, and Daniel Work. Automatic vehicle trajectory data reconstruction at scale. *arXiv preprint arXiv:2212.07907*, 2022.
- [45] S. K. Godunov. A finite difference method for the numerical computation of discontinuous solutions of the equations of fluid dynamics. *Mathematicheckii Sbornik*, 47:271–290, 1959.
- [46] Björn Engquist and Stanley Osher. One-sided difference approximations for nonlinear conservation laws. *Mathematics of Computation*, 36(154):321–351, 1981.
- [47] A. Aw and M. Rascle. Resurrection of "second order" models of traffic flow. *SIAM Journal on Applied Mathematics*, 60:916–938, 2000.
- [48] H Michael Zhang. A non-equilibrium traffic model devoid of gas-like behavior. *Transportation Research Part B: Methodological*, 36(3):275–290, 2002.
- [49] Geoff Langdale and Daniel Lemire. Parsing gigabytes of json per second. *The VLDB Journal*, 28(6):941–960, 2019.

## A Finite Volume Methods

Several finite volume-based numerical schemes are studied in this work. They include the following common classical first-order schemes:

**Godunov [45].**

$$\forall i, n \quad \hat{F}_{i-1/2}^n = \begin{cases} \min_{[u_{i-1}^n, u_i^n]} f & \text{if } u_{i-1}^n \leq u_i^n \\ \max_{[u_i^n, u_{i-1}^n]} f & \text{if } u_{i-1}^n > u_i^n \end{cases}$$

**Lax-Friedrichs [7].**

$$\forall i, n \quad \hat{F}_{i-1/2}^n = \frac{1}{2} (f(u_i^n) + f(u_{i-1}^n)) - \frac{1}{2} \frac{\Delta x}{\Delta t} \times |u_i^n - u_{i-1}^n|.$$

**Engquist-Osher [46].**

$$\forall i, n \quad \hat{F}_{i-1/2}^n(u_{i-1}^n, u_i^n) = \frac{1}{2} (f(u_i^n) + f(u_{i-1}^n)) - \frac{1}{2} \int_{u_{i-1}^n}^{u_i^n} |f'|.$$

Additionally, higher-order schemes such as the **Essentially Non-Oscillatory (ENO) method** [9] and the **Weighted Essentially Non-Oscillatory (WENO) method** [10] are considered. The main idea in these methods is that by considering more stencils, one can expect to increase the accuracy of approximation of the solution.

For the ENO scheme, we consider the semi-discrete form of

$$\partial_t u_i = -\frac{1}{\Delta x} (\hat{F}_{i+1/2} - \hat{F}_{i-1/2}). \quad (6)$$

Using the Lax-Friedrichs Splitting technique, we have

$$f(u) = f^+(u) + f^-(u), \quad f^\pm(u) = \frac{1}{2}(f(u) \pm \alpha u), \quad (7)$$

where  $\alpha = \max|f'(u)|$  is the maximum wave speed. The key point in the ENO scheme is the high-order upwind interpolation of  $f^+$  and  $f^-$  based on the smoothest stencils. For instance, for the 2-stencil ENO scheme, the procedure is as follows:

1. Evaluate the smoothness indicators:

$$\delta_- = |f_i^+ - f_{i-1}^+|, \quad \delta_+ = |f_{i+1}^+ - f_i^+|$$

2. Select the stencil that minimizes the smoothness indicator:

- If  $\delta_+ < \delta_-$ , choose the stencil  $\{f_i^+, f_{i+1}^+\}$ .
- Otherwise, choose the stencil  $\{f_{i-1}^+, f_i^+\}$ .

3. Perform linear interpolation to compute the numerical flux:

$$\hat{f}_{i+\frac{1}{2}}^+ = f_i^+ + \frac{1}{2} \delta^+$$

where  $\delta^+$  is the difference between the selected stencil elements.

A similar approach is applied to compute  $\hat{f}_{i+\frac{1}{2}}^-$  using the right-biased stencil.

The final numerical flux at the interface is obtained by combining the positive and negative parts:

$$\hat{f}_{i+\frac{1}{2}} = \hat{f}_{i+\frac{1}{2}}^+ + \hat{f}_{i+\frac{1}{2}}^-$$

In this work, we have used a 3-stencil scheme for ENO.

The WENO scheme follows the same idea as ENO by using specific weights in defining  $\hat{f}_{i+1/2}^+$ , rather than explicit conditions. In this work, we use the 5-stencil WENO scheme.

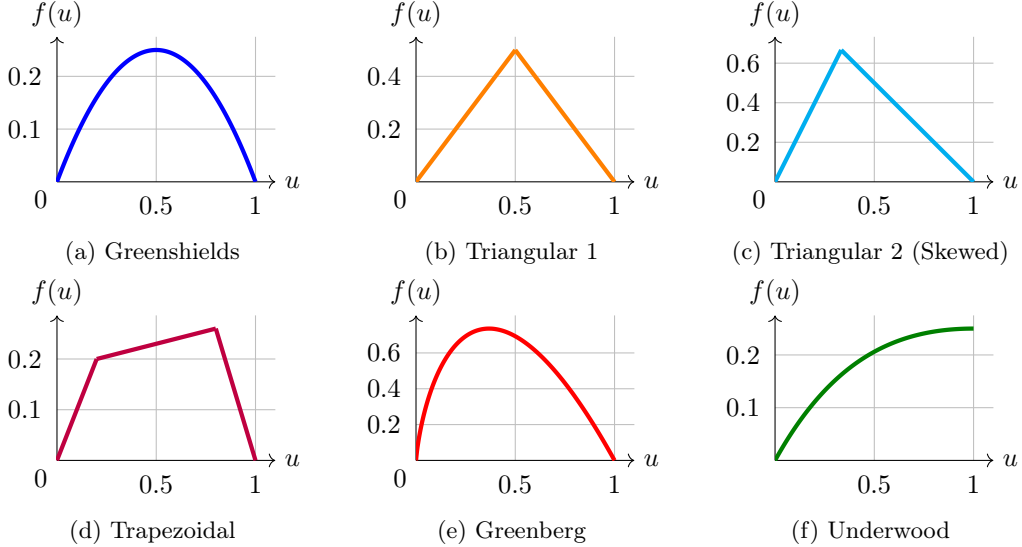


Figure 7: **Flow models for LWR.** We consider six different variants of the LWR PDE with the flows illustrated here, each mapping road density (veh/m) to traffic flow (veh/s).

## B Variants of LWR

We consider six different LWR PDEs variants, each consisting of a different fundamental diagram, illustrated in Figure 7. All of the considered flows are concave continuous mappings from  $[0, \rho_{\max}]$  to  $\mathbb{R}_+$ , where  $\rho_{\max}$  is the maximum density, with the exception of the Greenberg flow whose domain is  $(0, \rho_{\max}]$ . The critical density  $\rho_c$  denotes the density at which the flow is maximized, i.e.  $\rho_c = \arg \max_{\rho \in [0, \rho_{\max}]} f(\rho)$ . The following introduces the six flow models we consider in this work, each time detailing the flow's parameters, the parameter values we use in Section 5 (in parentheses), and the flow's definition. Note that we consider normalized parameter values lying between 0 and 1 for the most part.

**Greenshields.** Parameters: free-flow speed  $v_{\max}$  (1 m/s), maximum density  $\rho_{\max}$  (1 veh/m).

$$f(\rho) = v_{\max} \rho \left( 1 - \frac{\rho}{\rho_{\max}} \right)$$

**Triangular 1 (symmetrical).** Parameters: free-flow speed  $v_{\max}$  (1 m/s), critical density  $\rho_c$  (0.5 veh/m), maximum density  $\rho_{\max}$  (1 veh/m), wave propagation speed ( $-1$  m/s).

$$f(\rho) = \begin{cases} v_{\max} \rho & \text{if } \rho < \rho_c \\ w(\rho - \rho_{\max}) & \text{if } \rho \geq \rho_c \end{cases}$$

**Triangular 2 (skewed).** A non-symmetric variant of the Triangular flow, with parameters  $v_{\max} = 2$  m/s,  $\rho_c = 1/3$  veh/m, and  $w = -1$  m/s.

**Trapezoidal.** Parameters: free-flow speed  $v_{\max}$  (1 m/s), first density cusp  $\rho_1$  (0.2 veh/m), second density cusp  $\rho_2$  (0.8 veh/m), maximum density  $\rho_{\max}$  (1 veh/m), wave propagation

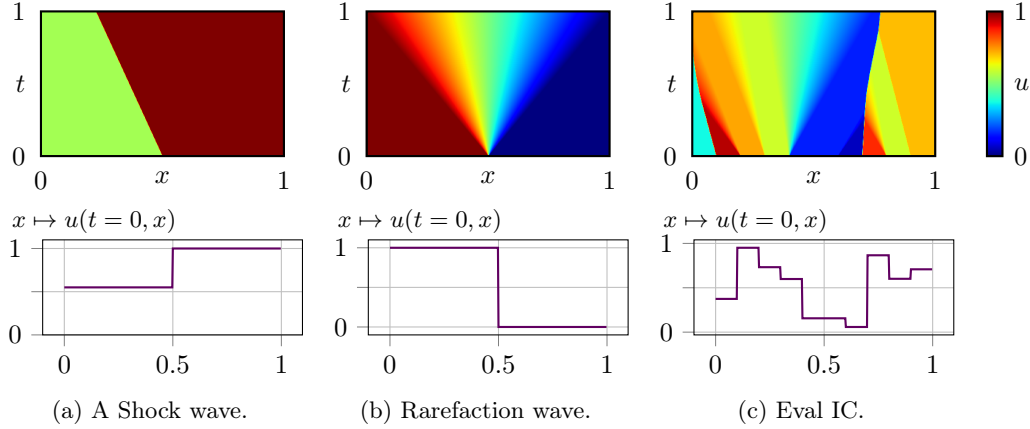


Figure 8: Exact solution for two Riemann problems (left, middle) and one piecewise-constant initial condition (right) from the evaluation set.

speed ( $-1.5$  m/s).

$$f(\rho) = \begin{cases} v_{\max}\rho & \text{if } \rho < \rho_1 \\ (w(\rho_2 - \rho_{\max}) - v_{\max}\rho_1) \frac{\rho - \rho_1}{\rho_2 - \rho_1} + v_{\max}\rho_1 & \text{if } \rho_1 \leq \rho \leq \rho_2 \\ w(\rho - \rho_{\max}) & \text{if } \rho > \rho_2 \end{cases}$$

**Greenberg.** Parameters: maximum density  $\rho_{\max}$  (1 veh/m), coefficient  $c_0$  (2).

$$f(\rho) = c_0 \rho \log(\rho_{\max}/\rho)$$

**Underwood.** Parameters: maximum density  $\rho_{\max}$  (1 veh/m), coefficients  $c_1$  (0.25) and  $c_2$  (1).

$$f(\rho) = c_1 \rho \exp(1 - c_2 \rho)$$

Example solutions of the Greenshields LWR are shown on various initial conditions in Figure 8.

## C More General PDE Models

### 2D Conservation Laws

A general form of conservation law equations in higher dimension can be written as

$$\begin{cases} \partial_t u + \nabla \cdot f(u) = 0 \\ u(0, x) = u_{\circ}(x) \end{cases} \quad (8)$$

for  $(t, x) \in \mathbb{R}_+ \times \mathbb{R}^n$ , initial condition  $u_{\circ}$ , and  $f : \mathbb{R} \rightarrow \mathbb{R}^n$ . The Riemann solution for such model in higher dimension does no longer exist. Therefore, the unsupervised approach can be very helpful in this case.

### Conservation Laws with Discontinuity in the Flux

A more general case of equations of conservation laws will include flux with dependence on the space variable. More precisely,

$$\begin{cases} \partial_t u(t, x) + \partial_x f(\gamma(x), u(t, x)) = 0 \\ u(0, x) = u_{\circ}(x). \end{cases} \quad (9)$$

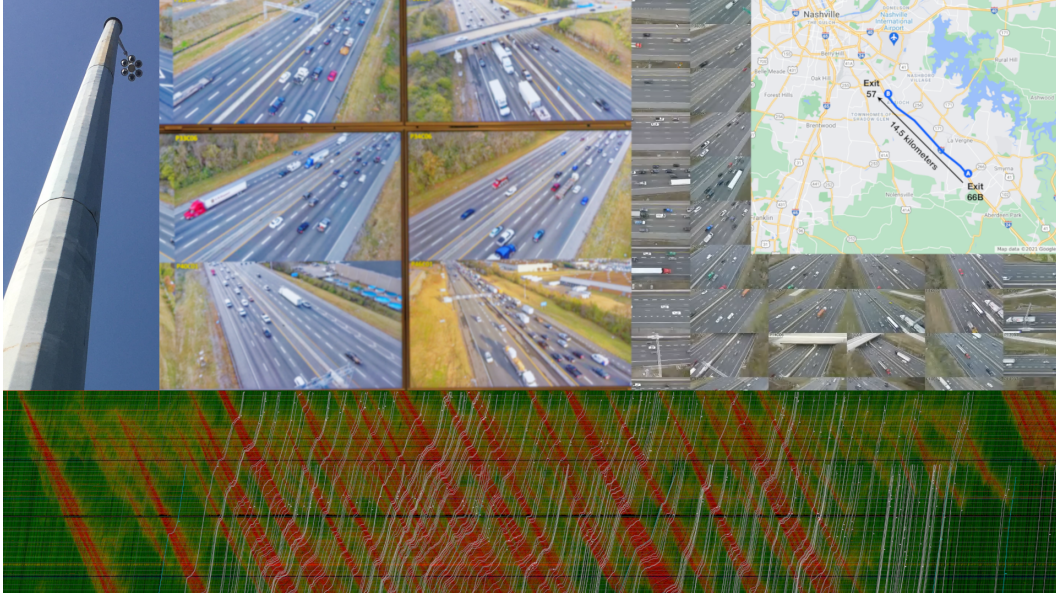


Figure 9: **I-24 MOTION** illustration. High-definition camera poles are mounted along a portion of I-24 at regular intervals. This generates massive amounts of video data, which is processed through a software stack. The resulting data for a single day is shown in the time-space diagram, displaying thousands of individual vehicle trajectories color-coded by speed (red for low speeds, green for high speeds), illustrating the complexity of the dataset.

Such equations are more complex in nature due to the discontinuity of the flux function and consequently lack some analytical properties such as bounded variations. However, in the one-dimensional model, the Riemann solution can still be defined.

### ARZ-Type Equations

The conservative form of the Aw-Rascle-Zhang (ARZ) equations [47, 48] can be written in the form of

$$\begin{cases} \partial_t \rho + \partial_x(\rho u) = 0 \\ \partial_t(\rho(u + p(\rho))) + \partial_x(\rho u(u + p(\rho))) = 0 \end{cases} \quad (10)$$

where  $\rho$  is density,  $u$  is the velocity function and  $\rho \mapsto p(\rho)$  is known as pressure term. In particular, the first equation represents the mass conservation, while the second equation models the conservation of momentum.

## D I-24 Experimental Dataset: Density Extraction, Training, and Evaluation

### D.1 Density Fields Extraction From I-24 MOTION Dataset

I-24 MOTION is a large-scale traffic monitoring system installed along a section of Interstate 24 near Nashville, Tennessee. It uses a dense network of high-resolution cameras and computer vision algorithms to capture detailed, real-time vehicle trajectories across multiple lanes and miles of highway. The data collection network and resulting trajectory data are illustrated in Figure 9.

For our experiments, we use the INCEPTION dataset<sup>1</sup> [42] from I-24 MOTION, consisting

<sup>1</sup>Available at [i24motion.org](http://i24motion.org) as part of the INCEPTION data release.

of ten days of data, each covering the morning rush hour (6:00 AM to 10:00 AM). The dataset for each day comprises 15-20 GB stored as a single JSON file. We first split each file into manageable 1 GB chunks and parse them efficiently using `simdjson` [49], which enables extraction of density fields in approximately 3-5 minutes per 20 GB file.

To construct the density fields, we discretize the spatiotemporal domain into cells of size 0.02 miles ( $\approx 32$  meters) in space and 0.1 seconds in time, aggregating data across all four lanes. Vehicle counts in each cell are normalized to obtain densities in vehicles per kilometer per lane. To reduce noise, we average over 100 consecutive time steps (i.e., 10 seconds) and over 2 adjacent spatial cells (i.e., 0.04 miles or  $\approx 64$  meters). This results in a grid of 100 spatial cells (4 miles / 0.04 miles) and approximately 1440 time steps (4 hours / 10 seconds). We clip the first and last segments of each day to exclude low-density, free-flow regimes with incomplete data, retaining 1300 time steps per day depending on data quality. To avoid extreme outliers, we cap densities at 140 vehicles/km/lane. For all training and evaluation purposes, we then normalize densities so that the maximum density is 1.

Due to occasional sensor failures, such as malfunctioning camera poles or occlusions by bridges, there are seven spatial locations with missing data. We fill these gaps by linear interpolation between the adjacent upstream and downstream cells.

Figure 10 shows the density fields we extracted from I-24 MOTION data. Higher densities (in red) correspond to stop-and-go waves and congestion, while lower densities (green) correspond to free-flow traffic. The processing code and resulting data are available in our codebase.

We exclude data from November 24 and 25, 2022, from our analysis, as both days correspond to holiday periods with purely free-flow, low-traffic conditions and no observable stop-and-go waves. These days are therefore not relevant to our study, which focuses on modeling traffic dynamics in the presence of congestion. The remaining days still include sufficient free-flow segments to evaluate model robustness in those regimes. Nevertheless, we include the excluded days in the released dataset for completeness.

## D.2 Boundary Conditions

For both training and evaluation of NFV on the I-24 dataset, we initialize the model using a single time step of real data and provide one boundary cell at each end of the road, using the corresponding real values. While it is possible to use additional ground truth data to improve accuracy, we deliberately restrict ourselves for two main reasons: (1) to allow fair comparison with the Godunov scheme, which uses a single boundary cell per side, and (2) to reflect realistic deployment scenarios, where boundary densities might only be measured at a few fixed points (e.g., at the road extremities), or predicted using a separate model.

For models that require a wider input stencil (e.g., those larger than  $\text{NFV}_3^1$ ), we pad the boundaries by duplicating the available single-cell values. This ensures that all models, no matter their size-Godunov,  $\text{NFV}^3$ , or  $\text{NFV}^{11}$ <sup>11</sup>—receive the same amount of boundary information. Figure 11 illustrates the boundary setup in both cases, showing which values are provided as an input and which are left to be predicted.

Finally, we emphasize that initial and boundary conditions are not included when computing metrics, whether in the training loss or at evaluation.

## D.3 Reading the Heatmaps

This section provides a brief explanation and intuition for interpreting the heatmaps displaying I-24 MOTION data. The horizontal axis represents time, increasing from left to right, while the vertical axis represents space along the road, increasing from bottom to top. The color encodes traffic density, normalized between 0 and 1, according to the colormap shown in Figure 12, where green indicates low density traffic (free flow) and red indicates high density traffic (congestion). Unless otherwise specified, only the model predictions are shown,

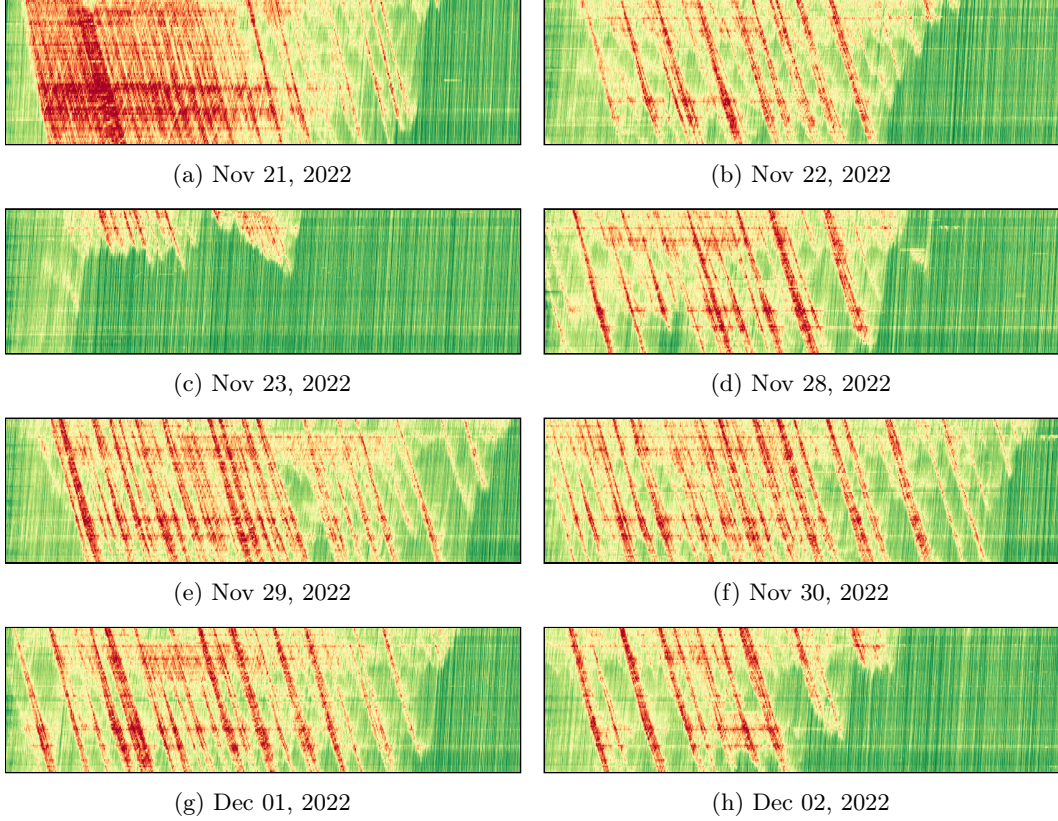


Figure 10: Time-space diagrams of car trajectories extracted from the video, colour-coded by density, for different dates. See Appendix D.3 for how to read the heatmaps.

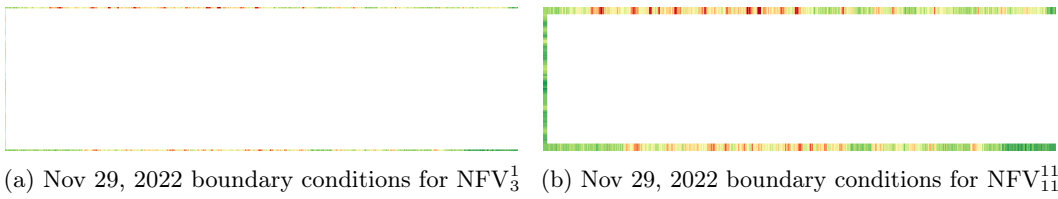


Figure 11: **Boundary conditions used by NFV during training and evaluation on the I-24 dataset.** The figures show the input provided to the model: the initial condition at  $t = 0$  on the left, and boundary conditions at  $x = 0$  (bottom) and  $x = x_{\max}$  (top). The model must then predict the interior (i.e., the region shown in Figure 10) autoregressively: it uses its own output at time  $t$  to predict the state at time  $t + dt$ , without receiving any additional data beyond the fixed boundaries. Note that both figures use the same underlying data; for  $\text{NFV}_{11}^{11}$ , the boundary values are duplicated to provide the required input padding.

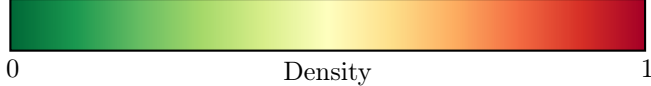


Figure 12: Colorbar showing density scale for all I-24 data heatmaps.

while initial and boundary conditions are omitted for clarity. Stop-and-go waves appear as high-density (red) bands that propagate upstream, i.e., move backward through traffic.

#### D.4 Predictions

Predictions on the training day from Section 6.2 are displayed in Figure 13. Predictions on evaluation days are displayed in Figure 14.

### E Experiment details

**Model Architecture.** The model is applied locally on each cell to estimate the corresponding numerical flux. It is implemented as a one-dimensional CNN. The first layer uses a kernel of size  $a - 1$ , followed by five 1D convolutional layers with 15 channels and kernel size 1. Using a CNN enables efficient vectorized computation over all stencils, which is equivalent to sliding a fully connected network along the input but significantly faster. Each time step is represented as a separate input channel, for a total of  $b$  input channels. The output is a single channel providing the estimated flux.

**Training on Synthetic Data (LWR).** For the LWR model, training is performed autoregressively: the model predicts future time steps by feeding its own outputs as inputs. To mitigate error accumulation, the prediction horizon is gradually increased from 10 to 250 steps during training. Initially, most training uses a 10-step horizon, which already yields satisfying performance. Fine-tuning with longer horizons improves stability. The model is trained with the Adam optimizer and an exponentially decaying learning rate, from  $10^{-4}$  to  $10^{-8}$ . Training is done on an RTX 6000 GPU and takes approximately 30 minutes.

**Dataset.** 400 Riemann problems are randomly sampled for training, with discretization parameters  $\Delta t = 5 \cdot 10^{-3}$  and  $\Delta x = 10^{-2}$ , with 100 space cells and up to 250 time steps. Training details can be found in Appendix E. A finer grid is used to compute the 100 test cases for evaluation using the Lax-Hopf algorithm:  $\Delta t = 10^{-4}$  and  $\Delta x = 10^{-3}$  with 200 cells and 1,000 time steps.

**Training on Experimental Data.** All models and fitted finite volume schemes are trained on the first hour of data from November 29, 2022 (arbitrarily selected), and evaluated on the full morning period (nearly four hours) and the remaining days of data. To ensure fairness and reflect practical deployment constraints, each model receives only a single boundary cell on each side, as described in Appendix D.2, even though larger models could benefit from additional context. Each NFV model consists of 6 hidden layers of width 15, totaling  $1105 + 16 \cdot ((a - 1) \cdot b + 1)$  parameters for  $\text{NFV}_a^b$ . Training takes 15 to 30 minutes on an RTX 4080 GPU. As with synthetic data, the prediction horizon increases progressively during training, from 10 to 100 steps, and the learning rate decays from  $10^{-3}$  to  $10^{-4}$  over 3000-5000 epochs depending on model size, until convergence.

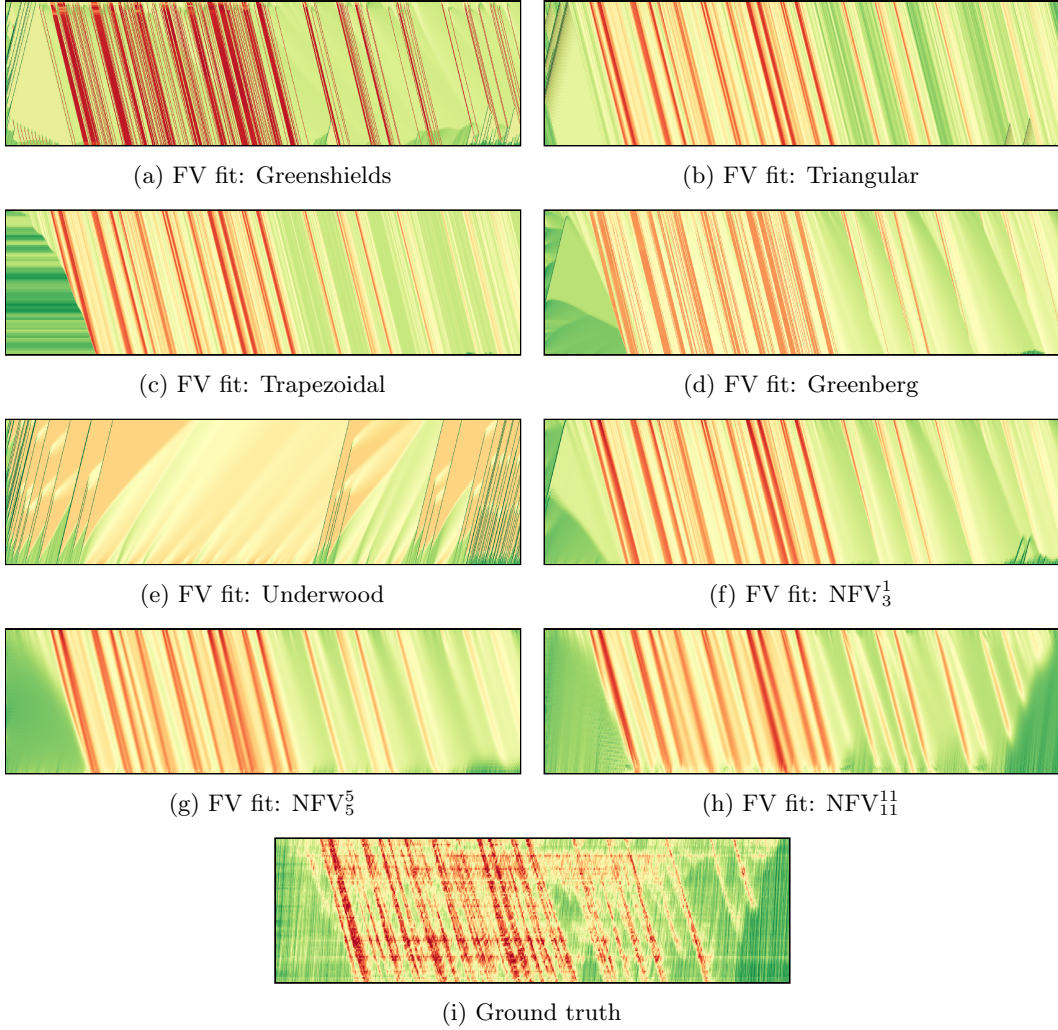
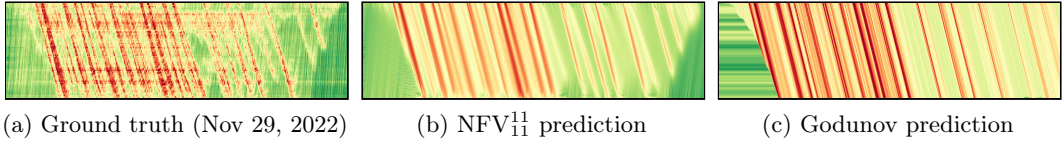
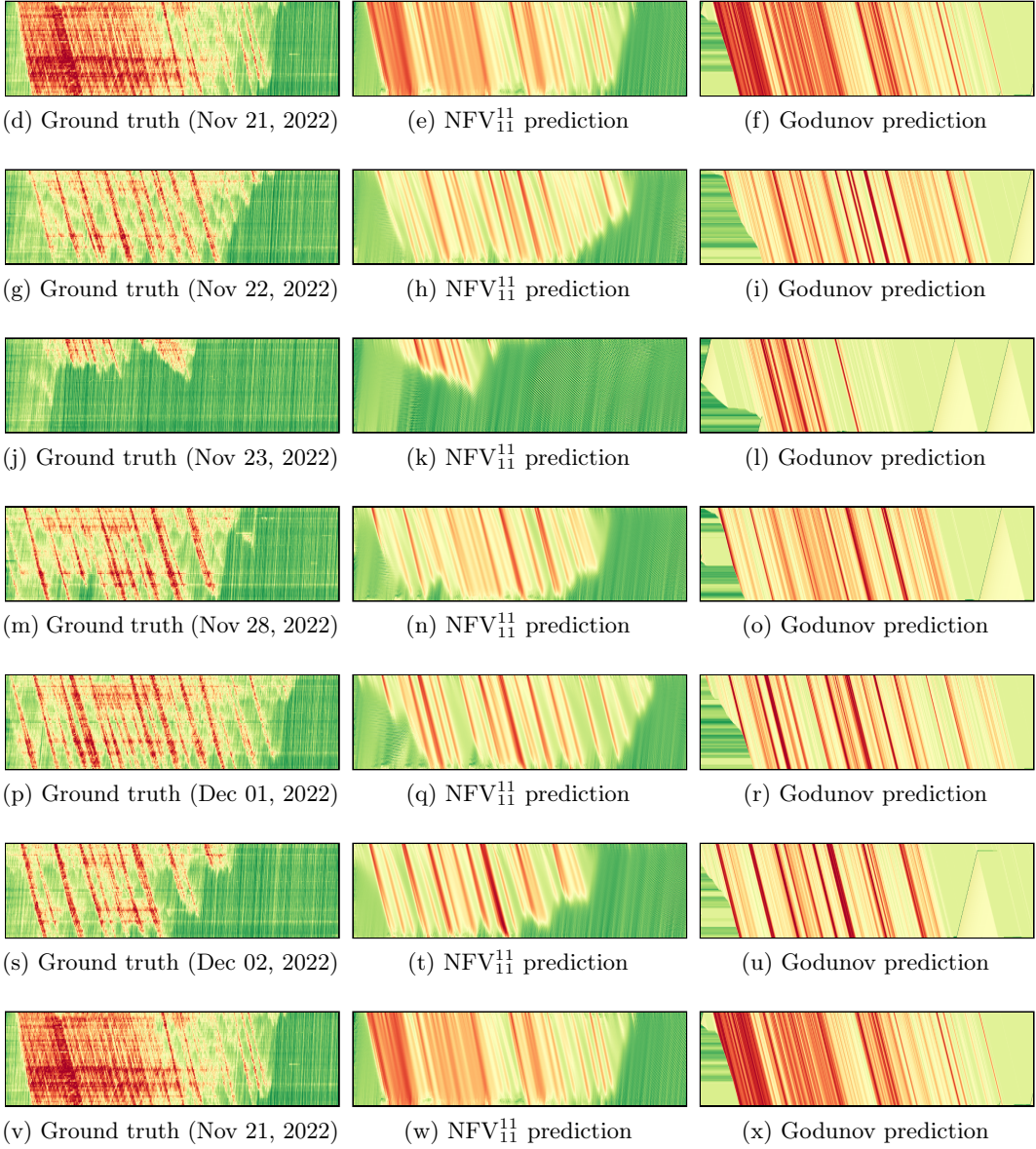


Figure 13: **Predictions of FV methods and trained NFV.** Corresponding metrics are reported in Table 3. Among the FV methods, only the Triangular, Trapezoidal, and Greenberg flows provide a reasonable fit to the I-24 MOTION data. In contrast, NFV models show increasing predictive accuracy with model complexity. For example,  $\text{NFV}_{11}^{11}$  captures significantly more stop-and-go waves (in red) than  $\text{NFV}_5^5$  or  $\text{NFV}_3^1$ , as well as fast low-density waves (in green), enabling it to correctly predict the early dissipation of the final two waves. However, it exhibits oscillations toward the end of the prediction window, likely due to limited generalization caused by the scarcity of low-density (dark green) patterns in the training data; nevertheless, the primary objective when modeling experimental data is to accurately capture the evolution of congestion waves, whereas free-flow traffic is of lesser interest. All models were trained on only the first 25% of the ground truth sequence, and the predictions are generated fully autoregressively. See Appendix D.3 for how to read the heatmaps.

**Prediction on training day**



**Generalization on unseen days**



**Figure 14: Predictions of best FV fit and trained  $\text{NFV}_{11}^{11}$ .** Godunov is derived by fitting a flow function on the prediction and comparing it against the ground truth; we keep the fitted Trapezoidal flow as it performed best (see Figure 13 and Table 3). Both the Godunov fit and the  $\text{NFV}_{11}^{11}$  training are realized using the same data, namely the first 1 hour of Nov 29, 2022 data (i.e., the first 25% of subfigure (a)). This means that the remainder of the data on that day (row 1), as well as the prediction on all subsequent days (rows 2-8) are generalization on data that was never seen before by either models. See Appendix D.3 for how to read the heatmaps.